TRANSPORT IN HIGH-PERFORMANCE PLASMAS OF THE T.J-II **STELLARATOR: FROM** FIRST-PRINCIPLES **SIMULATIONS** TO **EXPERIMENTAL VALIDATION**

- J. M. García-Regaña[†], D. Alegre¹, J. Alonso¹, J. A. Alonso¹, R. Antón¹, E. Ascasíbar¹, A. Baciero¹,
- J. M. Barcala², M. Barnes³, S. Barquero¹, E. Blanco¹, M. Borchardt⁴, L. Bueno¹, A. Bustos¹, S. Cabrera¹,
- A. de Castro¹, E. de la Cal¹, I. Calvo¹, A. Cappa¹, D. Carralero¹, R. Carrasco¹, B. Carreras⁵, R. Castro¹,
- A. de Castro¹, L. Cebrián¹, A.A. Chmyga⁶, M. Chamorro¹, J. Duque¹, F.J. Escoto^{1,12}, T. Estrada¹, A. Fernández¹,
- J. Fraguas¹, J.M. Fontdecaba¹, L. García³, I. García-Cortés¹, R. García-Gómez¹, G. Godino¹, J. Gómez-Manchón¹, A. González-Jerez¹, V. Guisse¹, J. Hernández-Sánchez¹, J. Hernánd
- P. Ivanova⁷, A. Jiménez-Denche¹, D. Jiménez-Rey¹, R. Kleiber, G. Kocsis⁸, M. Koepke⁹, A.S. Kozachek⁶,
- F. Lapayese¹, M. Liniers¹, D. López¹, D. López-Bruna¹, B. López-Miranda¹, E. de la Luna¹,
- E. Maragkoudakis¹, F. Martín-Díaz¹, G. Martín-Gómez¹, J. Martínez-Fernández¹, K.J. McCarthy¹, F. Medina¹,
- D. Medina-Roque¹, M. Medrano¹, P. Méndez¹, F.J. Miguel¹, B. van Milligen¹, A. Mishchenko⁴,
- A. Molinero², A. Mollén¹³, G. Motojima¹⁰, S. Mulas¹, M. Navarro¹, I. Nedzelskiy¹¹, R. Nuñez¹, M. Ochando¹,
- E. Oyarzábal¹, J.L. de Pablos¹, F. Palomares¹, N. Panadero¹, F. I. Parra¹², C. Pastor¹, I. Pastor¹,
- A. de la Peña¹, R. Peralta¹, A. Pereira¹, P. Pons-Villalonga¹, A.B. Portas¹, E. Poveda¹, F.J. Ramos¹,
- G.A. Rattá¹, M. Redondo¹, C. Reynoso¹, E. Rincón¹, J. de la Riva¹, C. Rodríguez-Fernández¹, A. Ros¹,
- C. Salcuni¹, E. Sánchez¹, J. Sánchez¹, E. Sánchez-Sarabia¹, S. Satake¹⁰, J.A. Sebastián¹, E.R. Solano¹,
- A. Soleto¹, T. Szepesi⁸, F.L. Tabarés¹, D. Tafalla¹, H. Takahashi¹⁰, N. Tamura^{4,10}, H. Thienpondt¹,
- A. Tolkachev¹, V. Tribaldos⁵, R. Unamuno¹, J. Varela¹⁴, J. Vega¹ and J.L. Velasco¹.

Abstract

We provide an overview of activities carried out at the TJ-II stellarator aimed at understanding transport from first principles and power balance analysis. These tasks include gyrokinetic simulations with the codes stella and EUTERPE, neoclassical simulations with the code SFINCS, particle deposition calculations with the code HPI2, and heat source estimates with ASCOT5. All these numerical simulation efforts converge, together with transport analyses, to address the transport mechanisms in plasmas with improved confinement through pellet injection—a scenario studied during the past few TJ-II campaigns bearing resemblance to the pellet-fueled high-performance plasma scenarios of observed in W7-X.

1. INTRODUCTION

In stellarators and tokamaks, transport of energy, particles, and momentum in the plasma core largely determines the performance of the device. Since the advent of stellarator optimization through computational design, configurations with increasingly improved transport properties have been obtained. The largest example built to date is the Wendelstein 7-X (W7-X) stellarator, which has successfully demonstrated reduced neoclassical transport and bootstrap current as a result of this

¹ Laboratorio Nacional de Fusión, CIEMAT, Madrid, Spain

² Technology Department, CIEMAT, Madrid, Spain

³ Rudolf Peierls Centre, University of Oxford, Oxford, UK

⁴ Max-Planck-Institut für Plasmaphysik, 17491 Greifswald, Germany

⁵ Universidad Carlos III, Madrid, Spain

⁶ Institute of Plasma Physics, NSC KIPT Kharkov, Ukraine

⁷Bulgarian Academy of Sciences, Sofia, Bulgaria

⁸ Centre for Energy Research, Budapest, Hungary

⁹ Physics and Astronomy Dpt, West Virginia University, USA

¹⁰ National Institute for Fusion Science, Toki, Japan

¹¹ IPFN, Instituto Superior Técnico, Univ. Lisboa, Lisboa, Portugal

¹²Princeton Plasma Physics Laboratory, Princeton, USA

¹³KTH Royal Institute of Technology, Stockholm, Sweden

¹⁴Institution for Fusion Studies, The University of Texas at Austin, Austin, USA

[†]E-mail: jose.regana@ciemat.es

optimization approach [Beidler-21]. However, the optimization of W7-X is insufficient with respect to some aspects in the path towards stellarator reactors, such as fast-ion confinement and turbulent transport. Recently, configurations with lower fast ion losses or reduced turbulent transport have been obtained, see e.g. [Sánchez-23, García-Regaña-25, Goodman-24, Kim-24] and references therein. Nonetheless, once a stellarator is built and its magnetic geometry is fixed, further confinement improvement can be attained by identifying advanced operation scenarios in which so-called enhanced or high performance is achieved. From this perspective, enhancing our understanding of the phenomena present in high-performance scenarios of current experiments is highly relevant.

The history of access to high-performance regimes in magnetically confined plasmas is extensive. Practically all present-day magnetic confinement devices, as well as many already decommissioned experiments, have reported confinement states with improved performance indicators—in comparison to what could be considered standard conditions—such as increased energy confinement time, reduced impurity accumulation, or diminished turbulence levels. The first milestones within the tokamak and stellarator families were achieved in ASDEX [Wagner-82] and, a few years later, in W7-AS [Erckmann-93], respectively. Subsequent advances in stellarator research include the discovery of the high-density H-mode in W7-AS [McCormick-02], a regime with distinct characteristics—such as the absence of ELM activity and reduced impurity concentration—not observed in the initial H-mode found in the same device. Also noteworthy are scenarios with record ion temperatures and the formation of internal transport barriers obtained in LHD plasmas [Takahashi-18]. In the case of the device addressed in this contribution, TJ-II, multiple pathways have been reported throughout its extended operation. Among the most remarkable are scenarios including L-H transitions triggered by turbulence suppression through sheared flows [Estrada-09] under Li-coating wall conditions [Sánchez-10].

Within the broad variability of operational parameters explored in different devices to achieve improved plasma performance—such as the use of heating systems above a certain power threshold, the excitation of electric field shear layers, the employment of impurity injection, etc.—W7-X and TJ-II share the particle fueling scheme of cryogenic hydrogen pellet injection as a key element in recently identified scenarios of interest. In particular, confinement improvements induced by pellet injection—first reported in [García-Cortés-21] and further extended in [McCarthy-24]—have been added to the list of enhanced-performance scenarios in TJ-II. This scenario resembles the one also found in W7-X [Bozhenkov-20], where pellet injection enables overcoming the barrier to increasing core ion temperature, commonly referred to as ion temperature clamping [Beurskens-21].

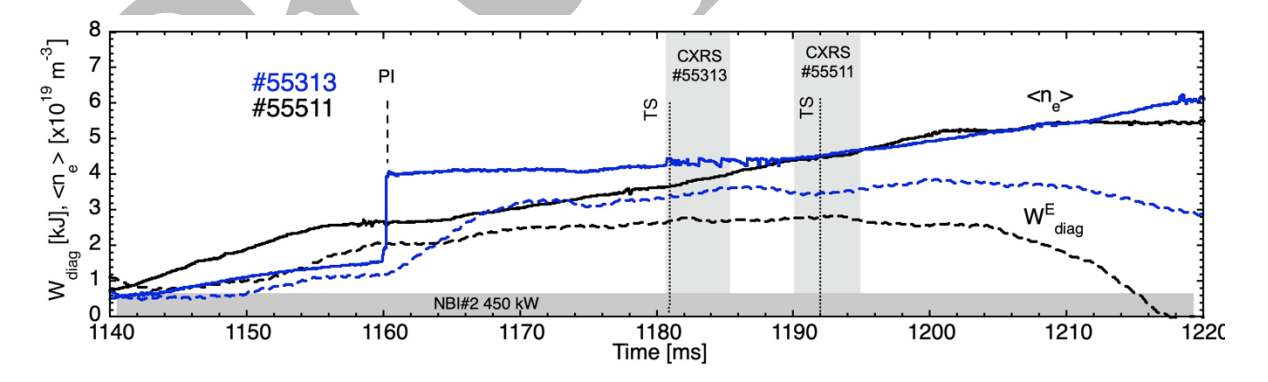


Figure 1. Time traces of line-averaged density (solid lines) and stored diamagnetic energy (dashed lines) for TJ-II discharges #55511 (without pellet injection, black) and #55313 (with pellet injection applied at 1160 ms, blue). Thomson scattering (TS, vertical dot line) and charge exchange recombination spectroscopy (CXRS, shaded grey) are carried out when the line-averaged densities in both discharges are close to 4.4×10^{19} m⁻³.

The reduction of fluctuations observed in W7-X during the post-pellet phases [Estrada-21], where a pronounced increase in the density gradient is produced compared with other scenarios [Carralero-21], is consistent with the strong turbulence reduction that such an increase in the density gradient drives—more so in W7-X than in any other device, according to gyrokinetic simulations (see, for example,

[García-Regaña-21, Thienpondt-25]). However, as we shall see, the same explanation does not appear to explain that clearly the confinement improvement observed in the pellet-fueled scenario of TJ-II. In this contribution, which builds on the collective experimental work carried out in recent years to realize these scenarios, we address an aspect that has scarcely been explored, namely their analysis through first-principles simulations.

We focus on two discharges reported in [McCarthy-24], in particular the discharges #55511 and #55313. Both follow a similar sequence: the plasma is initiated with an ECRH phase with 450 kW of injected power, followed by an NBI heating phase of the same power. In this NBI phase, while discharge #55511 serves as a reference, a pellet containing approximately 2.3×10^{19} hydrogen atoms is injected in discharge #55313, leading to an evolution with signatures of improved confinement. At similar lineaveraged densities, discharge #55313 shows higher stored energy (~3.6 kJ vs. 2.9 kJ in #55511, an increase of nearly 25%) and approximately 45% rise in central ion temperature (from ~115 eV to ~165 eV), with elevated T_i across all normalized minor radii up to $\rho = 0.8$ (for further details, we refer the reader to [McCarthy-24]). The time traces of diamagnetic energy and line-averaged density for both discharges are shown in figure 1. Figure 2 further displays the density and electron temperature profiles measured with the Thomson Scattering (TS) system, together with the ion temperature profiles obtained from Charge eXchange Recombination Spectroscopy (CXRS). Also shown are the fitted profiles used in the subsequent simulations, as well as the normalized gradients and selected ratios relevant to the discussion of transport in these discharges. As seen in figure 2, the regime accessed after the pellet injection does not produce a uniform increase in the density gradient across the entire radial range: below $\rho = 0.6$ it causes an increase, whereas at more external positions it leads to a relaxation. Regarding the temperature profiles, although the central electron temperature is practically unaffected, its gradient is decreases appreciably in the case with pellet. The opposite occurs with the ion temperature profile, where the gradient does not change significantly but its magnitude increases in the case with pellet, which leads to a decrease in the temperature ratio T_e/T_i as well.

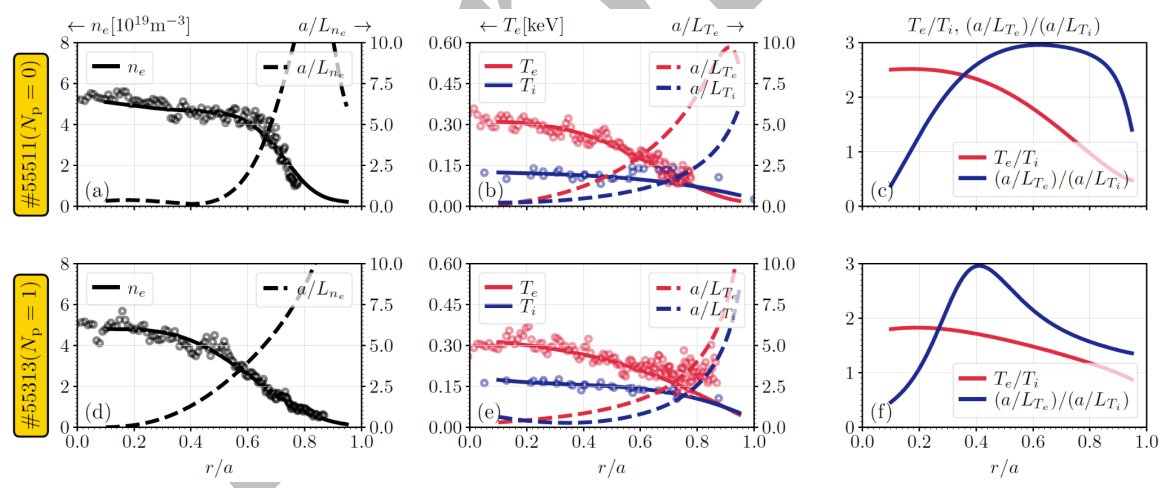


Figure 2: In the top row, density profiles (a), ion and electron temperatures (b), and the electron-to-ion temperature and temperature gradient ratios (c) for the discharge without pellet injection (#55511). In the corresponding bottom subfigures (d)–(f), the same quantities are shown for the discharge with pellet injection (#55313). The dashed lines represent the normalized gradients of the quantities plotted in the same figure.

The present contribution is structured into four main parts. First, we present a set of gyrokinetic simulations, performed with the stella code [Barnes-19], and neoclassical simulations, carried out with the SFINCS code [Landreman-14], using the fitted profiles shown in figure 2, with the aim of identifying the possible causes underlying the enhanced confinement features observed in discharge

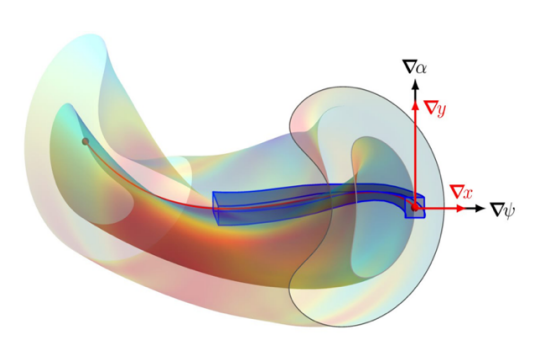


Figure 3: Segment of the flux tube used for the stella simulations at r/a = 0.5 of the TJ-II standard configuration. One eighth of its toroidal domain is shown together with the directions the radial and binormal coordinates; for further details, see [Barnes-19] and [Thienpondt-25].

#55313. Section 3 examines the effect of pellet injection on the density profile, evaluated with the HPI2 code in its stellarator version [Panadero-23]. Section 4 provides an analysis performed with the ASCOT5 code [Hirvijoki-14, Mulas-22] to quantify the heating contribution of the NBI system sustaining the phase of interest in these discharges. Section 5 presents a transport analysis similar to that conducted in W7-X (see, for example, [Carralero-22]). Finally, a summary is presented in Section 6.

2. PELLET-INDUCED ENHANCED CONFINEMENT THE LIGHT OF FIRST NEOCLASSICAL AND GYROKINETIC SIMULATIONS

The reduction or enhancement of heat transport and fluctuations, or the mitigation of instabilities, has attracted considerable attention in the field of simulations in recent times. In gyrokinetic simulations,

it has been observed that in the particular case of W7-X there exists a region where electrostatic instabilities upon exiting the ITG-unstable regime, do not respond with an excessive increase of density-gradient-driven instabilities [Alcusón-20]. This feature becomes much more pronounced in nonlinear simulations, where heat fluxes decrease with density gradient to a much greater extent than the linear growth rates do [Thienpondt-25]. This extraordinary reduction of heat losses with increasing density gradient over a broad range of values, and its evident potential for the operation of future stellarators, has even been found to be further enhanced (compared to the W7-X case) in newly optimized configurations according to gyrokinetic simulations; see, for example, [García-Regaña-25] or [Guttenfelder-25]

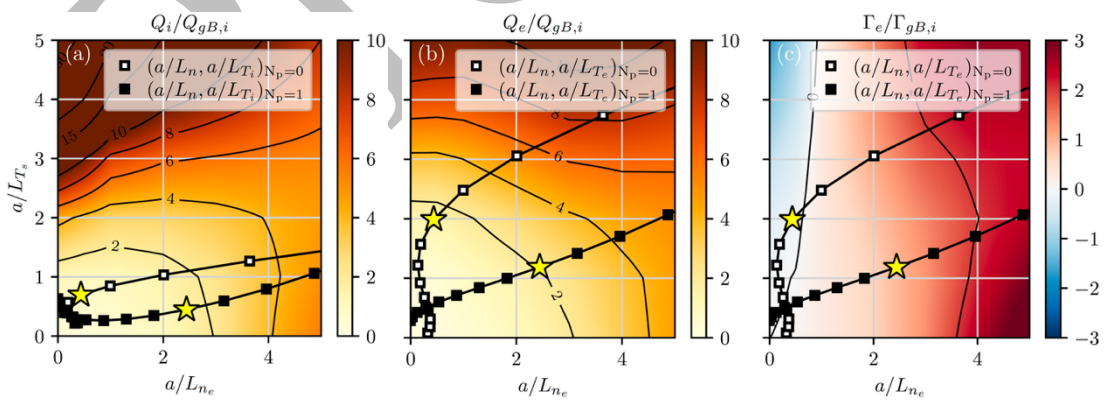


Figure 4: Turbulent ion heat flux (a), electron heat flux (b), and particle flux (c) as functions of the background species' density and temperature gradients for the radial position r/a = 0.5. The lines with open squares and filled squares represent, for shots #55511 (no pellet) and #55313 (1 pellet), respectively, the pairs of normalized density and ion temperature gradients in (a), and normalized density and electron temperature gradients in (b) and (c). The stars highlight the gradient values at the position r/a = 0.5. The spacing in r/a between consecutive points is 0.05.

In the present section, by means of electrostatic and collisionless gyrokinetic simulations with stella, we examine whether the turbulent fluxes computed for the two discharges under consideration—the

reference case (#55511) and the pellet-fueled one (#55313)—are consistent with the observed enhanced confinement signatures. Although simulations including third species, in addition to the bulk plasma, have shown reduction effects in cases with impurities [García-Regaña-24] or fast particles [di Siena-2020], in this section we restrict ourselves to a plasma composed solely of hydrogen ions and electrons. The simulations have been carried out for the flux tube illustrated in figure 3 at the position r/a = 0.5 (and the corresponding equivalents at the other radial locations considered) extended over a full poloidal turn. The turbulence scales cover a range from a radial wavenumber of $k_x \rho_i = 0.05$ up to $k_x \rho_i = 0.05$ up to $k_x \rho_i = 0.05$ up to $k_x \rho_i = 0.05$ up to the thermal Larmor radius of the main ions.

Figures 4(a)–(c) show the normalized ion heat flux, Q_i , electron heat flux, Q_e , and particle flux, Γ_e , as functions of the density gradient, a/L_{n_e} , and the temperature gradients, a/L_{T_s} , obtained from the simulations at r/a = 0.5. To guide the discussion, the pairs of gradients, $(a/L_{n_e}, a/L_{T_i})$ or $(a/L_{n_e}, a/L_{T_e})$, from the fits to the experimental data, shown in figure 2, are superimposed on these maps as lines. Looking at figures 4(a) and 4(b), and in particular at the color scale, one would expect a reduction of ion and electron heat losses with decreasing density gradient rather than with its increase. On the other hand, considering the location of the gradients of the two sets of profiles, it is consistent with the experimental situation that profiles of the non-pellet case steps on regions of higher fluxes, especially in the case of Q_e . Regarding particle transport, a stronger presence of the profile of the nopellet case is observed in the turbulent pinch region up to $r/a \approx 0.5$, which is in apparent contradiction with the fact that this case exhibits a flatter profile. However, as the radial coordinate increases, the represented points penetrate more rapidly into the strong outward particle transport region, which is consistent with the formation of a steeper gradient at edge positions, as is observed when comparing the profiles of the two discharges in figures 1(a) and 1(d). Nevertheless, this qualitative picture neglects the fact that the ion and electron temperature density gradients are not coupled in the discharges, nor are their respective gradients, see figures 1(c) and 1(f), and assumes that the color map is the same independently on the position.

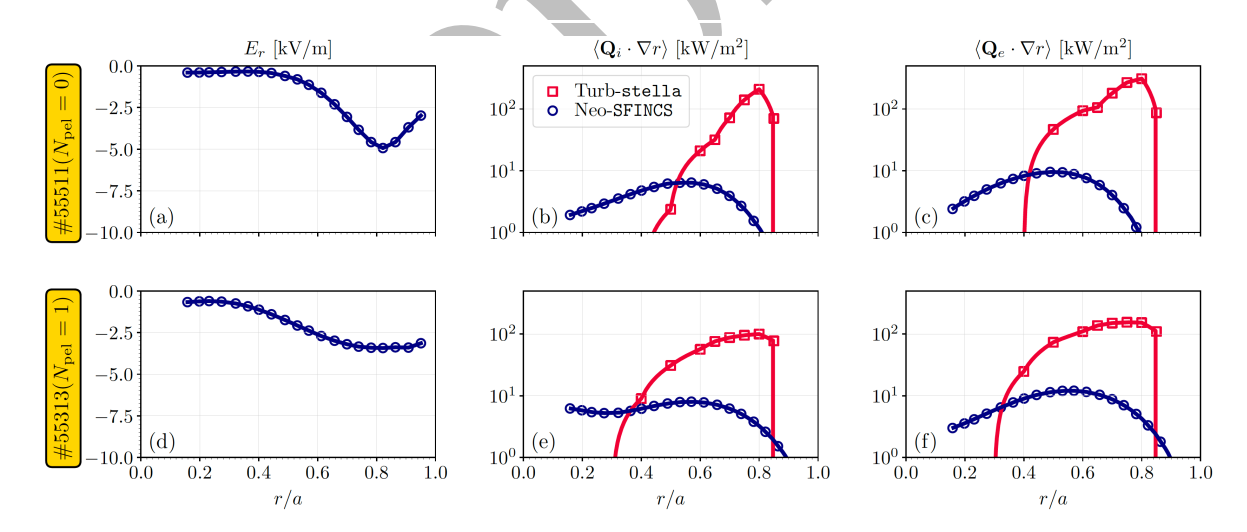


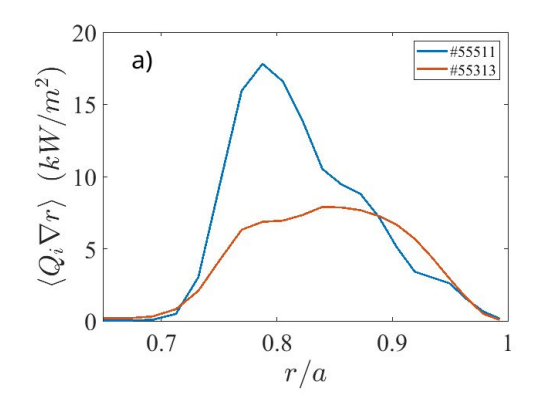
Figure 5: In the top row, as a function of the normalized minor radius, the neoclassical electric field (a), and the neoclassical and turbulent ion (b) and electron (c) fluxs re shown for the discharge without pellets (#55511). In the bottom row, the same quantities are shown for the discharge with a single pellet injection (#55313).

Therefore, turning to a quantitative description, preliminary stella simulations using the fitted profiles are shown in figure 5, adding neoclassical calculations performed with SFINCS. A somewhat larger radial electric field is observed for the pellet case than for the non-pellet case up to $r/a \approx 0.6$, beyond which the trend is reversed. Regarding the heat fluxes, the turbulent components—both ion and electron—clearly exceed the neoclassical ones from intermediate radial positions outward, consistent with transport analyses presented for TJ-II and compared with neoclassical calculations in [Dinklage-

2013]. Moreover, while the pellet case exhibits a reduction of the peak turbulent heat fluxes the heat flux profiles are broader than the non-pellet case. Nevertheless, the reduction of the fluxes in the inner region is not sufficient to compensate for the larger flux observed at the outermost simulated positions of the discharge without pellets.

When the turbulent fluxes are integrated over the simulated region, although the total value is overestimated (if we take into acount the upper bound set by the NBI heating source estimated in section 4 with ASCOT4), the relative difference between scenarios amounts to about 20% higher in the non-pellet discharge compared to the pellet case. This result is consistent with the fact that the energy confinement time improves by a similar amount when pellets are injected.

Finally, the larger flux in the peripheral plasma region for the pellet scenario is also captured by global simulations performed with EUTERPE [Kleiber-24], also in electrostatic regime and accounting for kinetic electrons and main ions with mass ratio $m_e/m_i = 1/200$. This feature is evident in figures 6(a) and 6(b), both for the electron heat flux and, even more prominently, for the ion heat flux.



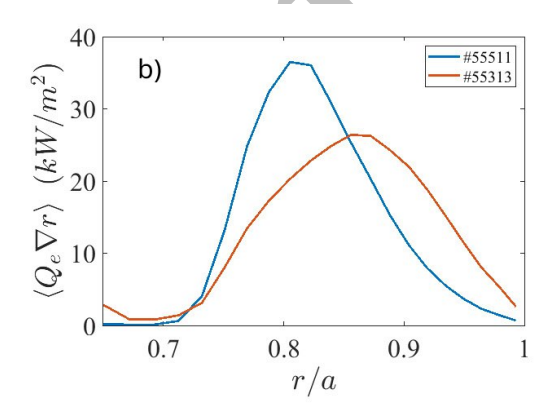


Figure 6: Ion (a) and electron (b) heat flux obtained with EUTERPE as a function of the radial coordinate in the peripheral region for the discharges with pellet (#55313, orange) and without pellets (#55511, blue).

Additional turbulence simulations that may provide a more complete picture are underway, taking into account profile uncertainties and the inclusion of further effects, such as collisions or the presence of impurities.

3. STUDY OF THE EFFECT OF THE PELLET ON THE DENSITY PROFILE

The transient changes in the density profile caused by these pellets may be responsible for the changes in transport that result in an improved plasma regime. In order to gain a better understanding of where the particles are initially deposited in the plasma, the HPI2 code [Pegourie-05, Pegourie-07], in its stellarator version [Panadero-23] is used to simulate a pellet injection under conditions similar to those presented here. In particular, discharge #55313 of the TJ-II is considered. For this simulation, the density and temperature measured by the Thomson scattering system in a similar discharge (#50095), close to the time of pellet injection, were used as input, together with the experimental pellet mass and speed (Thomson scattering measurements taken immediately prior to the injection of the pellet were not available for discharge #55313). It should be noted that some simplifications and assumptions have been made. Firstly, it is assumed that there is no pellet acceleration caused by suprathermal ions. This is often not the case, as strong toroidal deflection is commonly observed in TJ-II for pellets injected into NBI plasmas due to an imbalance in ablation. Therefore, while the nominal trajectory of this type of pellet crosses the magnetic axis, this may not be the case in the experiment, with particles being deposited at different radial positions. Unfortunately, a fast camera was unavailable for the cases presented here, so it is not possible to verify whether the deflection is significant. Additionally, the effect of fast ions in ablation is simplified by assuming a beam of mono-energetic suprathermal ions.

This simplification is not significantly relevant for the study's purpose as it should be sufficient to approximately reproduce pellet penetration and ablation profile, see figure 7. This figure shows ablation light, providing an estimation of the ablation rate, collected from above the pellet, and the ablation calculated by HPI2, both with and without the consideration of fast ions in the ablation process. It can be observed that the predicted ablation resembles the H_{α} from the ablation light fairly well, except for the peak between 0.11 m and 0.16 m from the plasma edge. Pellet penetration is estimated to be approximately 0.2 m, similar to the experimental penetration.

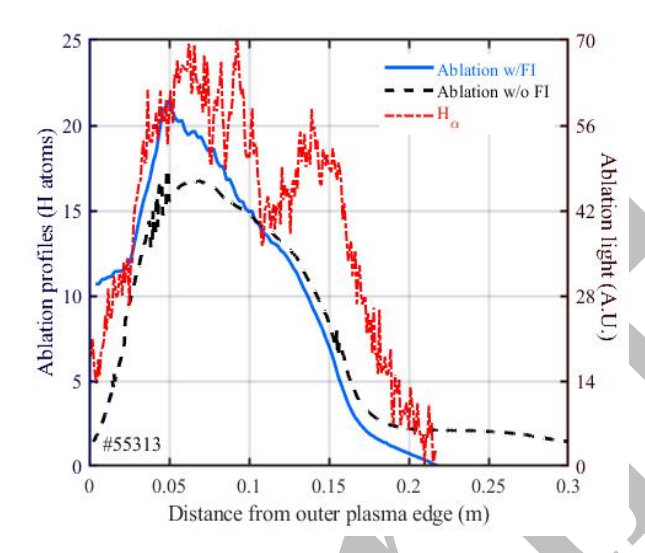


Figure 7. HPI2 simulated ablation profiles with (solid blue) and without (dashed black) fast ions are compared with the measured H α light (dash-dotted red) for a pellet injected nominally through the magnetic axis into the NBI2 phase of discharge #55313 with 2.3x10¹⁹ H atoms and velocity = 885 m/s.

In this case, the HPI2 code predicts that the pellet will create a peaked density profile, as can be seen in figure 8. There is a significant increase in core density since the pellet has penetrated deep enough to cross the magnetic axis. Additionally, ablation occurs for a significant fraction of the pellet lifetime in regions of the plasma that are beneficial in terms of fuelling. Furthermore, HPI2 predicts significant changes in the density gradients.

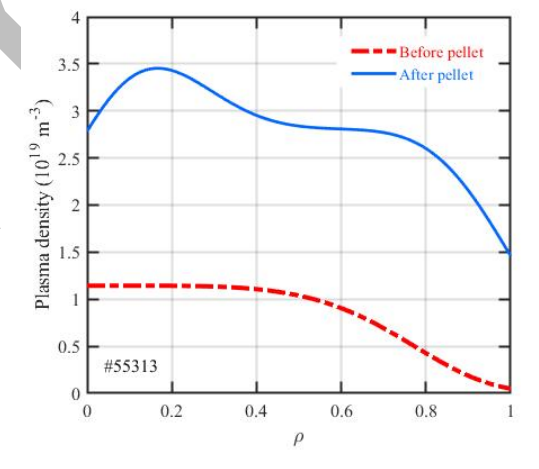


Figure 8. Plasma density before (dashed-dotted red, fitted from Thomson Scattering data from a similar discharge -#50095) and immediately after (solid blue, calculated by HPI2) a pellet injection in #55313 (2.3x1019 H atoms with a velocity of 885 m/s). It should be note that the simulated density shown here corresponds to the time just after a pellet is injected at 1160 ms, which is 35 ms before the time at which the profiles are measured and other simulations and analyses are performed.

4. STUDY OF THE NBI POWER SOURCE

The plasma in shots #55313 and #55511 is heated solely by hydrogen neutral beam injection, using the counter beam (NBI2). Both shots have very similar heating power and beam energy. We simulate the NBI injection in TJ-II with the ASCOT5 orbit following code [Mulas-22]. Table 1 shows the NBI injection parameters, as well as the available and total absorbed power for both shots.

The power deposition profiles, both for electrons and ions, are represented in figure 9. Between 70 and 75 % of the power is transferred to the electrons in these low temperature plasmas. The critical energy is around 4-5 keV, much lower than the beam characteristic energies.

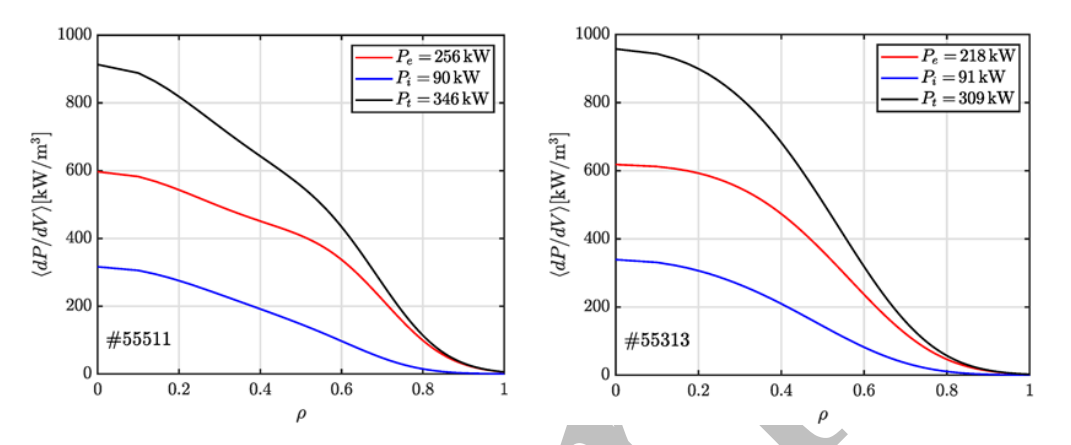


Figure 9: NBI power deposition profiles for the discharges without pellet injection (left) and for the discharge with pellet injection (right).

We have used $Z_{\rm eff} = 1$ and have not taken into account charge exchange losses. Both effects combined would reduce the heating efficiency and modify the proportion of power transferred to electrons and ions.

Shot#	P_{in} [kW]	Energy [keV]	P _{st} [%]	P_{av} [%]	P_{abs} [kW]
55511	470	31.5	11.3	88.7	346
55313	450	30.2	15.9	84.1	309

Table 1: Beam maximum energy and port-through (P_{in}) , shine-through (P_{st}) , available (P_{av}) and total absorbed power (P_{abs}) .

5. POWER BALANCE ANALYSIS

Once the NBI deposition has been evaluated, it is possible to evaluate the experimental energy transport for the two scenarios by means of power balance analysis. This technique has been widely used in the literature to study both transport in general and high performance scenarios in particular both in W7-X [Bozhenkov-20, Carralero-22, Wappl-25] and other stellarators [Stroth PPCF 98, Dinklage-13], but so far had never been used to provide quantitative estimations of transport in TJ-II. Power balance assumes a stationary state and integrates sinks and sources over each flux surface to evaluate the flux surface-averaged total heat flux for electrons/ions, $Q_{tot,e/i}$, by fulfilling energy continuity. For each species α , total heat flux can be described as the combination of a neoclassical and a turbulent component, $Q_{tot,\alpha} = Q_{NC,\alpha} + Q_{turb,\alpha}$. Since $Q_{NC,\alpha}$ has been numerically calculated with SFINCS (as shown in figure 5), the turbulent component can be readily obtained from $Q_{tot,\alpha}$.

In the case at hand, the two scenarios seem reasonably stationary, at least from the perspective of the total energy stored in the plasma (see figure 1). Therefore, density and temperature profiles are taken at t = 1186 for #55511 (no pellet) and t = 1182 for #55313 (one pellet). While accounting for the temporal variation of the profiles could add more precision to the calculation, this is not possible as both of the involved diagnostics (TS for electron density and temperature; CXRS for ion temperature) are effectively only capable of one measurement per discharge. As well, impurity confinement variations between the two scenarios have not been considered, taking a $Z_{eff} = 1.5$ value, based on spectroscopy measurements of a range of similar discharges. The only energy source in the plasma is the one created by the NBI injection, whose deposition profiles are taken from the ASCOT5 simulations described in the previous section. Regarding the sinks, line radiation and CX interactions with the neutrals crossing the LCFS remove energy respectively from electrons and ions in the edge. This is due to the lack of reliable measurements of the neutral density profile and the bolometry tomographic system being unavailable due to technical reasons. The first hypothesis underestimates energy losses in the ion channel, mostly in the edge region, while the second underestimates moderate losses in the electron channel over the whole radius. Nevertheless, since both discharges have similar density and electron temperature profiles, for a qualitative comparison between the two scenarios, it seems safe to assume that the contributions of these phenomena are roughly equal in both cases and can thus be ignored. In any case, the discussion will be limited to the central region ($\rho < 0.85$), where the results can be considered more reliable. Finally, collisional coupling between species must be considered as a heat/sink term $P_{ei} \propto n_e^2 T^{-3/2} (T_e - T_i)$. In the discussed scenarios this term transfers energy from the electrons to the ions, as $T_e > T_i$ due to the higher NBI deposition in the electrons. Unfortunately, this term is highly sensitive to small variations on the density and, crucially, to the temperature difference between species and thus severely affected by profile uncertainty. When evaluating $Q_{turb,e}$ within the profile errorbars, it is observed that there are regions of the plasma for which unphysical results $(Q_{turb,e} < 0$ appear within the confidence bounds. This is a common problem of this kind of analysis (see eg., the discussion in [Ford-24]), so given the indirect method to establish the absolute value of density after the pellet injection, the common solution of considering the total transport of both species (thus canceling out P_{ei}) has been adopted.

The results of the analysis are displayed in figure 10: as can be seen, turbulent transport is reduced in the scenario with pellet injection for $\rho > 0.55$, with the strongest effect being observed around $\rho \sim 0.75$. A similar evolution can be seen when the heat transport coefficient $\chi_{\alpha} \sim (2/3)Q_{\alpha}/(n_{\rm e}\nabla T_{\alpha})$ is normalized by the gyroBohm value, thus indicating that the reduction in transport is associated to a change in the transport mechanism in this region and not to a trivial consequence of the changes in thermodynamic gradients. It is noteworthy that the average change in transport in $0.75 > \rho > 0.65$ region is around 30%, which matches the scale of the confinement improvement with respect to the ISS04 scaling reported for the 1 pellet case in [McCarthy-24]. While qualitative, this result is in very good agreement with the outcome of the gyrokinetic simulations discussed in section 2, for which a similar drop between scenarios can be observed, also around $\rho \sim 0.75$.

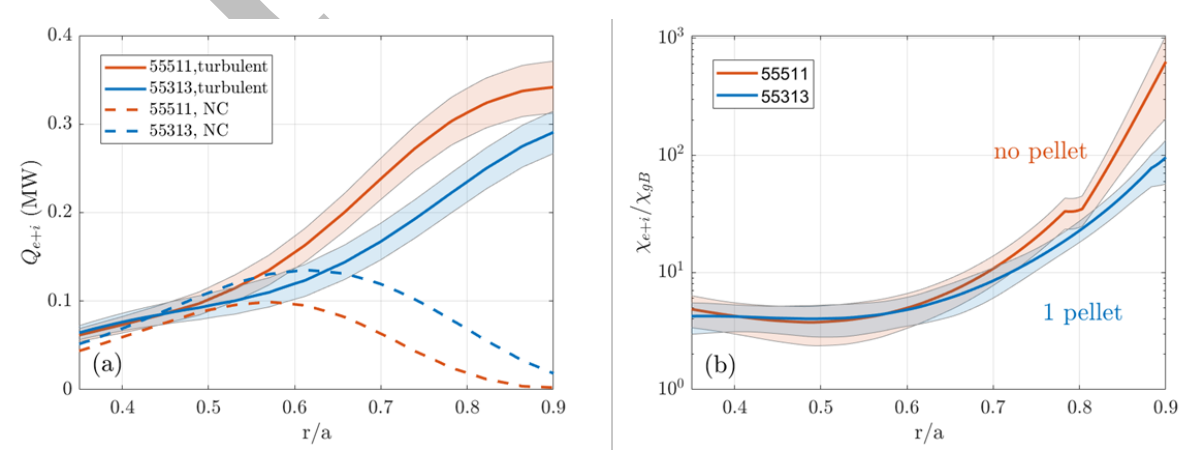


Figure 10. Experimental measurements of transport. In plot (a), radial profiles of the turbulent energy transport obtained by power balance analysis are shown for shots #55511 (no pellet) and #55313 (1 pellet) in red and blue.

Neoclassical values from SFINCS simulations are shown in dashed lines. In plot (b) thermal transport coefficients normalized to the gyroBohm values are shown for the same two cases.

6. SUMMARY

In the present work, we have provided a first comprehensive analysis—both through first-principles numerical simulations and experimental analysis—of the transport properties in pellet-induced enhanced confinement scenarios in TJ-II, taking as a starting point one discharge without and one with pellet injection. The most significant findings concern the effect of the pellet on the density profile, the differences in power deposition, and the predicted fluxes. Particularly significant is the evidence that the changes in transport observed by power balance are driven by modifications in the turbulent channel in the outer plasma region, as captured by gyrokinetic simulations and transport analyses.

ACKNOWLEDGEMENTS

This work has been carried out within the framework of the EUROfusion Consortium, funded by the European Union via the Euratom Research and Training Programme (Grant Agreement No 101052200—EUROfusion). Views and opinions expressed are however those of the author(s) only and do not necessarily reflect those of the European Union or the European Commission. Neither the European Union nor the European Commission can be held responsible for them.

REFERENCES

[Alcusón-20] J. A. Alcusón et al. Plasma Phys. Control. Fusion 62 035005 (2020)

[Barnes-19] M. Barnes et al., J. Comp. Phys. 391, 365 (2019)

[Beidler-20] Beidler et al., Nature 596, 221 (2021)

[Beurskens 2021] M.N.A. Beurskens et al. Nucl. Fusion 61, 116072 (2021)

[Bozhenkov-20] S. Bozhenkov et al., Nucl. Fusion 60, 066011 (2020)

[Carralero-21] D. Carralero et al. Nucl. Fusion 61, 096015 (2021)

[Carralero-22] D. Carralero et al. Plasma Phys. Control. Fusion 64, 044006 (2022)

[Erckmann 1993] V. Erckmann, et al. Phys. Rev. Lett. 70, 2086 (1993)

[Estrada-09] T. Estrada et al., Plasma Phys. Control. Fusion 51, 124015 (2009)

[Estrada-21] T. Estrada et al. Nucl. Fusion 61, 046008 (2021)

[Ford NF 24] O.P. Ford et al 2024 Nucl. Fusion 64, 086067 (2024)

[Goodman-24] A. G. Goodman et al. Phys Rev. X Energy 3, 023010 (2024)

[Hirvijoki-14] E. Hirvijoki et al. Comp. Phys. Comm. 185, 1310 (2014)

[Kim-24] P. Kim et al. J. Plasma Phys. 90, 905900210 (2024)

[McCarthy-24] K. J. McCarthy et al. Nucl. Fusion 64, 066019 (2024)

[McCormick-02] K. McCormick et al., Phys. Rev. Lett. 89, 015001 (2002)

[García-Cortés-23] I. García-Cortés et al., Phys. Plasmas 30, 092303 (2023)

[García-Regaña-21] J. M. García-Regaña et al. Nucl. Fusion Nucl. Fusion 61, 116019 (2021)

[García-Regaña-24] J. M. García-Regaña et al., Phys. Rev. Lett. 133, 105101 (2024)

[García-Regaña-25] J. M. García-Regaña et al. Nucl. Fusion 65, 016036 (2025)

[Guttenfelder-25] W. Guttenfelder et al. J. Plasma Phys. 91, E83 (2025)

[Kleiber-24] R. Kleiber et al. Comp. Phys. Comm. 295, 109013 (2024)

[Landreman-14] M. Landreman et al. Phys. Plasmas 21, 042503 (2014)

[Mulas-22] S. Mulas et al. Nucl. Fusion 62, 106008 (2022).

[Panadero-23] N. Panadero et al. Nucl. Fusion 63, 046022 (2023)

[Pégourié-05] B. Pégourié et al. Plasma Phys. Control. Fusion 47, 17 (2005)

[Pegourie-07] B. Pégourié et al. Nucl. Fusion 47, 44 (2007)

[Sánchez-09] J. Sánchez et al. Nucl. Fusion 49, 104018 (2009)

[Sánchez-23] E. Sánchez et al., Nucl. Fusion 63, 066037 (2023)

[Stroth-98] U. Stroth Plasma Phys. Control. Fusion 40, 9 (1998)

[Takahashi-18] H. Takahashi et al., Nucl. Fusion 58, 106028 (2018)

[Thienpondt-25] H. Thienpondt et al., Nucl. Fusion 65, 016062 (2025)

[Thienpondt-23] H. Thienpondt et al., Phys. Rev. Res. 5, L022053 (2023)

[Wappl-25] M Wappl et al. Plasma Phys. Control. Fusion, 67 075025 (2025)